

Leipzig University
Leipzig Institute for Meteorology

Silver - The program for
Stereographic Infrared reconstruction
of cLoud points with the airborne
VELOX imagER

Bachelor Thesis

Paul Rothenberg
Matriculation number: 3784558

First reviewer: Prof. Dr. Manfred Wendisch
Second reviewer: Dr. Michael Schäfer

Leipzig, 2025-06-26

“There is robust evidence and high agreement across a diverse range of modelling approaches and thus high confidence that radiative feedbacks are the largest source of uncertainty in projected global warming out to 2100 under increasing or stable emissions scenarios, and that cloud feedbacks in particular are the dominant source of that uncertainty.”

Sixth Assessment Report
Intergovernmental Panel on Climate Change

Contents

1	Introduction	3
2	The core of <i>Silver</i>	5
2.1	Brightness temperature datasets acquired through the VELOX imager	5
2.2	Generation of image pairs from VELOX brightness temperature datasets	6
2.3	Tracking of cloud points	6
2.3.1	Interpretation of a cloud surface point	6
2.3.2	Selection of reidentifiable points	7
2.3.3	Evaluation of the cloud point movement	8
2.4	Reconstruction of cloud points.....	9
2.4.1	Concept of the stereographic reconstruction.....	9
2.4.2	Overview of <i>Silver's</i> coordinate systems	11
2.4.3	Allocation of viewing directions.....	12
2.4.4	First reconstruction in calm air	13
2.4.5	Plausibility height filter	13
2.4.6	Iterative correction of the wind-cloud displacement	14
2.5	Resulting datasets	15
2.6	Geometric camera calibration	15
2.6.1	Pixel viewing direction in the camera system	15
2.6.2	Position of the camera system in the aircraft system	18
3	Evaluation for test cases	19
3.1	Comparison between Lidar and <i>Silver</i>	19
3.2	Lateral height stability.....	22
3.3	Behavior for visible ground.....	24
3.4	Low contrasts in the visible spectrum	25
4	Case study on cloud height progression during a cloud streets event	26
5	Conclusions	28

Abstract

Precise data regarding the vertical and horizontal positions of clouds and their three-dimensional structures are invaluable for the evaluation of atmospheric measurement campaigns and of great importance for the description of radiative transfer processes through the atmosphere. Due to limitations of existing measurement technologies, airborne stereography has recently been used to detect cloud surfaces. The foundation for this consists of image pairs that are captured with a meticulously calibrated camera and whose necessary parallax is formed by the movement of the aircraft. From this, the horizontal position and height of contrast-rich image points can be computed in three-dimensional space. Previous methods work with solar radiation and have the problem that this does not always produce sufficient contrasts, for instance at night or over bright surfaces. To overcome this issue, the program for Stereographic Infrared reconstruction of cLoud points with the airborne VELOX imagER (*Silver*) has been developed, which enables reconstruction using data from a camera operating in thermal infrared. In the process, the functionality and potential of this technique were demonstrated in several test cases, such as in comparison with lidar measurements, plus an additional case study on a cloud streets event. However, it also became clear that a few tweaks, including a more precise camera calibration, are still needed before it should be generally applied for scientific analyses on datasets collected during aircraft measurement campaigns. Once these obstacles have been overcome, *Silver* can precisely close important data gaps in cloud localization.

1 Introduction

The position and geometry of clouds provide a wide range of useful information that is especially beneficial when analyzing atmospheric measurement campaigns. The data is not only useful for describing the nature of the cloud field. It is also used to localize cloud properties determined by remote sensing instruments, i.e. to assign a precise location to measured variables. Furthermore, the geometry and orientation of a cloud plays a significant role in the derivation of radiative transfer properties as well as the effective droplet radius and the cloud droplet size distribution. Therefore, a precise determination is essential. All of this data can then help to improve the parameterizations of weather and climate models in order to optimize forecast quality.

The measuring instruments frequently utilized for this purpose include ceilometer or lidar systems, which can be used, for instance, to gauge the cloud base altitude. However, a measured profile usually only provides information about the position of one cloud point on the cloud structure. If the interest lies in the geometric properties of the cloud, such as shape, rotation and position, these instruments have to scan a large number of points, which is a technically complex and time-consuming process, further impeded by the cloud development over time. In the field of airborne remote sensing, this is hardly feasible due to the high aircraft velocity. The lidar and radar systems used here are usually pointing towards the nadir and only cover a small measurement volume. Help for this problem comes from passive remote sensing. Al-

though these instruments cannot utilize techniques such as time-of-flight differences like active remote sensing, they make it possible to capture a significantly larger measurement volume and therefore are ideal for deriving large-scale geometries. One of the better-known methods is the measurement of brightness temperatures. For instance, using an airborne, nadir-directed thermal infrared imager (Schäfer et al., 2022). If the atmospheric temperature profile is known, for example through dropsonde observations or model data, it is possible to draw a simplified conclusion about the height of the cloud top. Another technique, developed and described by Zinner et al. (2019), examines the absorption of radiation in the oxygen-A-band through an aircraft side window. This allows conclusions to be drawn about the distance and ultimately the position of cloud points.

In contrast, the method presented in this thesis is based on the principle of stereography. Stereography, also referred to as stereoscopy or stereo photography, is not a new approach and has been used successfully in technology for decades. In its basic principle, stereography describes the spatial impression that arises when an object is viewed from two different angles. This spatiality can be evaluated mathematically so that an exact position can be calculated. To do this, the locations of the two different viewpoints and the viewing directions must be known precisely. The major advantages of this method are its spectral independence and the relatively few assumptions that are required in order to derive the data. It is therefore not surprising that there are already ground-based systems for the purpose of cloud geometry derivation. By utilizing at least two cameras that simultaneously photograph a cloud from different angles, cloud points can be three-dimensionally localized. Spaceborne instruments, such as the Advanced Spaceborne Thermal Emission and Reflection Radiometer (ASTER) or the Multi-angle Imaging SpectroRadiometer (MISR) on board the Terra satellite, enable measurements from above, allowing data to be collected from the cloud tops. However, the large distance between the satellite and the cloud combined with a relatively long scanning time of around one minute per image pair results in considerable uncertainties.

Consequently, it is only a logical step to also utilize aircraft for this purpose in order to improve the data quality. To this end, Kölling et al. (2019) as well as Volkmer et al. (2024) have developed a procedure that makes it possible to reconstruct cloud points with a single airborne camera. The datasets obtained in this context using cameras from the spectrometer of the Munich Aerosol Cloud Scanner (specMACS; Ewald et al., 2016; Weber et al., 2024) were verified with lidar measurements, reanalysis data and simulations showing promising precision. The disadvantage of cameras operating in the visual spectrum is that this radiation is not always present and does not necessarily provide sufficient contrast, which is indispensable for stereographic analysis. Examples of such cases are measurement flights at night as well as overflights of bright backgrounds, which occur frequently in the polar regions. Since bright clouds can hardly be separated from a bright sea ice surface, data acquisition proves difficult.

For this reason, the program for Stereographic Infrared reconstruction of cLoud points with the airborne VELOX imagER (*Silver*) was developed to stereographically evaluate the brightness temperature data obtained by the VELOX327k veL imager. Like specMACS, this camera system is frequently installed on board the High Altitude

and LOng Range Research Aircraft (HALO). *Silver*'s underlying methodology is based on the publications by Kölling et al. (2019) and Volkmer et al. (2024), allowing a daylight-independent evaluation, which is also not affected by sunglints. Objects of visually the same color can be separated from each other as they usually show different brightness temperatures, which facilitates the detection of clouds over ice or snow surfaces.

This thesis is a feasibility study on stereographic reconstruction with the VELOX imager and a documentation for *Silver*. It describes the basic ideas, procedures and algorithms for deriving points on the cloud surface and the resulting datasets in Section 2. The quality is reviewed in Section 3 using several test cases from the HALO-(*AC*)³ campaign (ArctiC Amplification: Climate Relevant Atmospheric and SurfaCe Processes, and Feedback Mechanisms) and shows the current strengths and weaknesses of the system. Subsequently, a case study on cloud height progression during a cloud streets event has been conducted and is presented in Section 4.

2 The core of *Silver*

This section covers the complete theory needed to derive points on the cloud structure from brightness temperature raster data. It begins with a brief description of the VELOX data itself (Section 2.1). This is followed by the processing steps comprising the video generation (Section 2.2), point selection and tracking (Section 2.3), the reconstruction geometry (Section 2.4) and the resulting data sets (Section 2.5). It concludes with an overview of the imager calibration required for the analysis (Section 2.6).

2.1 Brightness temperature datasets acquired through the VELOX imager

The VELOX (Video airbornE Longwave Observations within siX channels; Schäfer et al., 2022) system is a nadir-directed, aircraft-based, passive remote sensing instrument that is specialized in the measurement of thermal infrared radiation emitted upwards by clouds and surfaces. It comprises the frequently mentioned VELOX imager (VELOX327k veL) and an infrared thermometer (KT19.85II).

For the stereographic analysis, the two-dimensional images obtained by the VELOX imager are of relevance. This imager has a rotating filter wheel to accommodate six filters, which is currently used to measure five different spectral channels. Each filter channel is captured with a temporal resolution of approximately 16 Hz. The published datasets from the HALO-(*AC*)³ campaign (Schäfer et al., 2023) provide a temporal resolution of 1 Hz, which is adequate for the reconstruction. Furthermore, the image edges are trimmed to ensure exact overlapping of the individual channels.

The stereographic processing is performed with channel 1 in the electromagnetic wavelength band of 7.70 μm to 12.00 μm , utilizing the atmospheric window region. This channel provides the largest spectral scope and thus the highest signal-to-noise ratio, which is important for generating sufficient image point contrasts necessary for the analysis, as explained in Section 2.3.2. The image sensor features a resolution of 640 px \times 512 px with a field of view of 35.5° \times 28.7°. Accordingly, one pixel covers

an area of approximately $10\text{ m} \times 10\text{ m}$ at a target distance of 10 km. Each pixel cell measures a value proportional to the detected photon count per unit time. Through multiple calibrations and corrections, the brightness temperatures can be derived from these values, with a precision better than 0.1 K.

2.2 Generation of image pairs from VELOX brightness temperature datasets

The basis for the identification of cloud points is the OpenCV software library (Bradski, 2000), which provides algorithms for computer vision. Hence, the first step is to convert the VELOX brightness temperature dataset into video files. *Silver* generates individual videos from this data, each containing two frames recorded with a time difference of one second. For each of these videos, a stereographic reconstruction can be performed. The second frame of a video corresponds to the first frame of the next video. To avoid videos with larger time intervals in the event of data gaps, the dataset is checked for temporal integrity. Since in the field of computer vision mostly grayscale-based algorithms are used, the videos also consist of grayscale images, which make full use of the contrast range for the best possible point recognition.

Regarding the later reconstruction, it is important to know that most video codecs only support an even number of pixel rows and columns due to compression algorithms. If the VELOX dataset has an odd quantity as a result of cropping, the pixels would regularly be remapped. This not only changes the original data, but also falsifies the viewing direction that is assigned to each pixel by a calibration. To avoid this, *Silver* must be provided with the parameter “vid_edge_trim”. This defines the number of pixels that are missing at each edge in the dataset in relation to the raw data. On this basis, an excess row or column of pixels is then removed to make the number even. The trimming is applied to the side with the smaller initial crop.

In contrast to the method developed by Kölling et al. (2019), the two-frame approach cannot track the same cloud points over several time steps. However, new, well-trackable points are searched for at each moment in time, which can lead to duplicates, but scans the cloud field as broadly as possible. Since the range of brightness temperature values can also become quite large and sometimes varies rapidly, contrasts in longer videos can often no longer be displayed as well, which would limit data acquisition.

2.3 Tracking of cloud points

2.3.1 Interpretation of a cloud surface point

For the interpretation of the measurement data, it is important to be aware of a fundamental characteristic of clouds. They have no clearly definable boundary, but represent a successive transition from a low to a high concentration of hydrometeors. The VELOX imager measures in a wavelength range of $7.70\text{ }\mu\text{m}$ to $12.00\text{ }\mu\text{m}$ (Schäfer et al., 2022) and thereby exploits the atmospheric window in which the typical gases of the atmosphere, including water vapor, are predominantly translucent. This means

that the detected thermal infrared radiation is emitted by liquid or solid objects in the air or on the ground. As for clouds, they become visible for the camera through the emission of thermal radiation by liquid water or ice. For the reconstruction of the cloud surface, it must be assumed that the visible boundary in the measured spectral range corresponds to the cloud boundary and that the term surface refers to the thermal infrared emitting envelope layer of the cloud. These prescriptions do not necessarily coincide with cloud microphysical gradients but indicate the interaction with thermal infrared radiation and therefore are interesting for properties that are dependent on it. With regard to reconstructed data generated by cameras operating in the visual spectrum, systematic deviations may occur due to the differently defined boundaries, i.e. to the differences in origin of the scattered solar and emitted thermal radiation. However, it remains to be seen whether these differences can be separated from the measurement uncertainties.

2.3.2 Selection of reidentifiable points

To identify a cloud point in two consecutive images, its apparent movement through the field of view has to be describable. For this reason, the pixels to be evaluated must provide contrasts in the two spatial dimensions with respect to the surrounding pixels, otherwise the aperture problem will occur. This phenomenon is schematically illustrated in Figure 1. If the black rectangle is observed, it is noticeable that it moves to the right in the time period from t_1 to t_2 , which is comparable with a very homogeneous cloud moving through the camera's field of view. Now individual cloud points should be identified and processed in order to derive the geometry as completely as possible. However, the algorithm can only evaluate individual pixels and their surroundings, meaning that it only sees a very small part of the overall image. If this section does not feature any contrasts, like the yellow square in the center of the rectangle, no change can be detected in this image fragment. The cutouts are identical for both time steps. Even with a contrast in only one spatial direction, such as the blue square at the lower edge of the rectangle, the movement cannot be

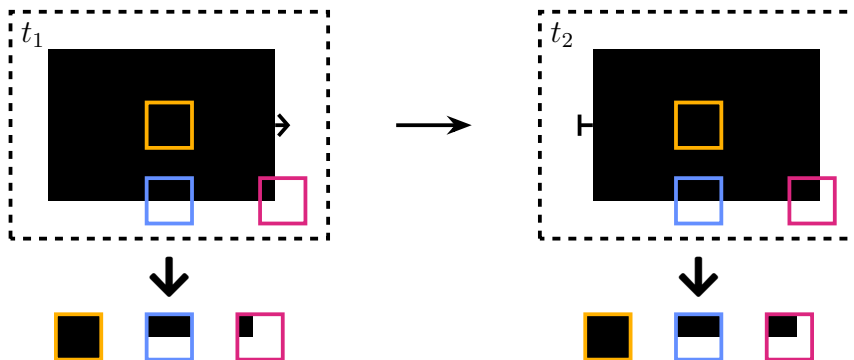


Figure 1: Schematic of the aperture problem, in which the underlying movement cannot be fully described when viewed through a small window. Three segments and their perspectives are highlighted. The movement of the black rectangle is only completely quantifiable if there are contrasts in both spatial dimensions, like at the corner.

fully described by just looking at this segment. It only becomes possible if there are contrasts in two spatial dimensions, like in the example at the corners. Then the movement can also be observed and fully quantified in the small magenta square.

To find such corners, *Silver* uses the Shi-Tomasi corner detection algorithm (Shi and Tomasi, 1994), which computes the Hessian matrix:

$$\mathbf{H} = \begin{bmatrix} \frac{\partial^2 I}{\partial x^2} & \frac{\partial^2 I}{\partial x \partial y} \\ \frac{\partial^2 I}{\partial y \partial x} & \frac{\partial^2 I}{\partial y^2} \end{bmatrix} \quad (1)$$

for each pixel. Here, I is the grayscale pixel intensity, x and y denote the two spatial directions in the two-dimensional image. A special feature of the Hessian matrix is that its eigenvalues provide information about changes in intensity. If both eigenvalues are significantly above zero, a corner has been found. To characterize the pixels, the quality criterion $\min(\lambda_1, \lambda_2)$ is used, where λ_1 and λ_2 represent the two eigenvalues. *Silver* was configured to require points to achieve at least a quality level of ten percent of the highest occurring quality score found in the image to be suitable for tracking. Furthermore, only a maximum of one thousand points per image pair are tracked to ensure that the dataset is not unnecessarily bloated and the computation time remains manageable. If there are more than a thousand suitable candidates, those with the higher quality value are selected. Since between the points a minimum Euclidean distance of five pixels is required in order to scan the cloud field as broadly as possible, this limit is rarely reached.

2.3.3 Evaluation of the cloud point movement

The promising cloud points selected in the first frame must also be identified in the second frame to allow for reconstruction. To achieve this, an optical flow algorithm is utilized. It evaluates the optical flow, i.e. the apparent movement in consecutive images. The basic principle is depicted in Figure 2. It shows a cloud point moving through the camera's field of view, shifting by dx and dy in the time period of t_1 to t_2 . It is now assumed that the point intensities do not change over the image pair. Under this condition, the optical flow equation:

$$0 = \frac{\partial I}{\partial x} u + \frac{\partial I}{\partial y} v + \frac{\partial I}{\partial t} \quad (2)$$

can be formulated (OpenCV, b). This advection equation comprises the grayscale pixel intensity I , the spatial coordinates x , y and the time t as well as the velocities u and v at which the point moves through the image. The velocities constitute the optical flow vector, which points to the position of the cloud point in the second image.

The problem with this equation lies in its two unknown variables u and v . Because of this, *Silver* uses the Lucas-Kanade method (Lucas and Kanade, 1981) with the pyramid implementation introduced by Bouguet (2001). The algorithm assumes that the adjacent pixels, i.e. a 3×3 array, perform the same movement. This results in nine equations containing only two unknown variables. Such a system is solvable, which is accomplished by applying a least squares method to optimally determine these parameters. The pyramid technique is necessary because the described algorithm

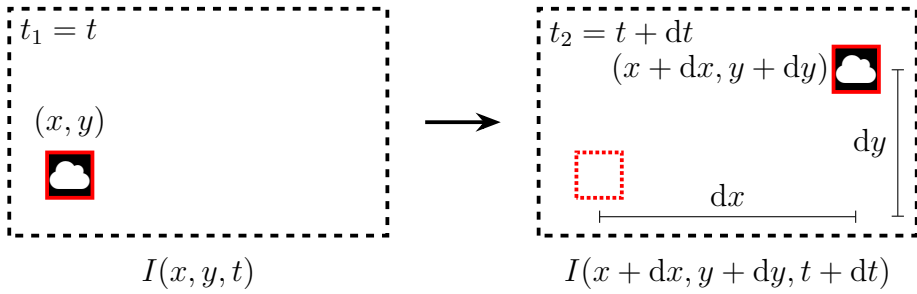


Figure 2: Concept of the optical flow. The observed cloud point moves in the period of t_1 to t_2 through the field of view with the dimensions x , y and retains its intensity I .

can only determine small movements in the sub-pixel range properly. If a point has moved across several image pixels, it will result in failure. To avoid this, the image resolution is reduced in cascades, whereby individual pixel patches are merged. Consequently, even large motions will eventually lie in the sub-pixel range and can be quantified. The flow vectors obtained on coarse scales form a starting point for resolving the flows on finer scales. The results provide the position of the cloud points in the second image. If the algorithm still does not find a match, the cloud point cannot be evaluated any further.

In reality, it is not always the case that the intensities of the tracked points remain the same over the image pair. It also happens that cloud points are no longer visible in the second image as they have already left the camera's field of view. In such cases, it is possible that the standard algorithm returns a similar looking point. As this is of course undesirable, the optical flow is calculated backwards for the purpose of quality assurance, which means that the flow is computed from the second to the first frame using the results obtained from the forward calculation as the starting point. For *Silver*, a point tracking is only successful if the deviation between the initial point and the back-calculated point is less than one pixel in the x and y directions.

2.4 Reconstruction of cloud points

2.4.1 Concept of the stereographic reconstruction

The basis of this measurement technique is a nadir-directed camera directly mounted to the aircraft. There must be no internal image stabilization enabled, as this would falsify the sensor readings and render them unusable for reconstruction. The camera must be calibrated in such a way that each sensor pixel can be assigned a viewing direction in the aircraft reference system.

Figure 3 shows the stereographic reconstruction scheme developed by Kölling et al. (2019) and Volkmer et al. (2024) which is implemented in *Silver*. At position P_1 , the aircraft takes a picture of the cloud, or more precisely, a cloud point. This cloud point lies within a pixel and can therefore be associated with a viewing direction. As the viewing direction is equivalent to a geometric ray, it is evident that the measured point must be located on this ray. After a defined flight time, which is one second in the case of the published VELOX data, a new image is captured at position P_2 . Due to the change in position, the viewing angle on the cloud and the previously observed

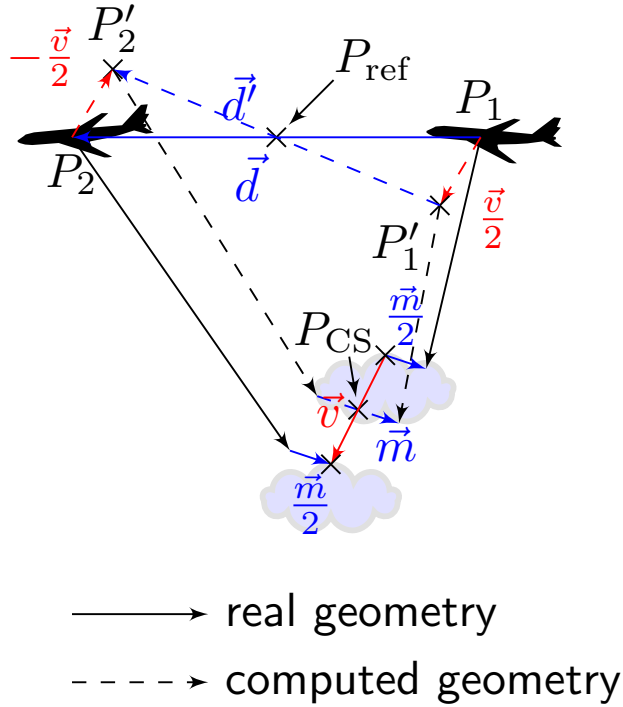


Figure 3: Reconstruction scheme as implemented in *Silver*. Solid lines represent the measured geometry, whereas dashed lines depict the geometry used in the processing. The points P_1 , P_2 and P'_1 , P'_2 are the real and virtual aircraft positions, P_{ref} is the origin of the stereo reference system, \vec{d} and \vec{d}' are the real and virtually flown distances, \vec{m} is the mis-pointing vector and \vec{v} is the wind vector at the mean cloud point P_{CS} . (Volkmer et al., 2024)

cloud point shifts. The point is now situated in a different pixel and consequently lies on a different ray. The time increment between the two images is a tradeoff, based on the knowledge that a larger parallax reduces measurement uncertainties, while allowing the clouds to develop over a longer time period, which can annihilate this effect. If the exact locations of the image recordings are known, the intersection of the two rays can be calculated and thereby also the precise position of the cloud point.

The problem that now arises in three-dimensional space is that there does not necessarily have to be an intersection point between two straight lines. Because of this, the so-called mis-pointing vector \vec{m} is introduced. It describes the shortest distance between the two rays. By definition, the considered cloud point is located at the center of this vector. Another problem is that the position and geometry of the cloud changes over the recording time due to factors such as wind or convection. At least the horizontal displacement can be taken into account under the assumption that the cloud travels with the horizontal wind. This is accomplished by shifting the aircraft position P_1 and P_2 with and against the half wind vector at the cloud point. Hence, the measurement takes place virtually at the points P'_1 and P'_2 . The viewing directions remain unchanged in the aircraft reference system. This results in the viewing vectors pointing to a common mean cloud point P_{CS} and cancels out

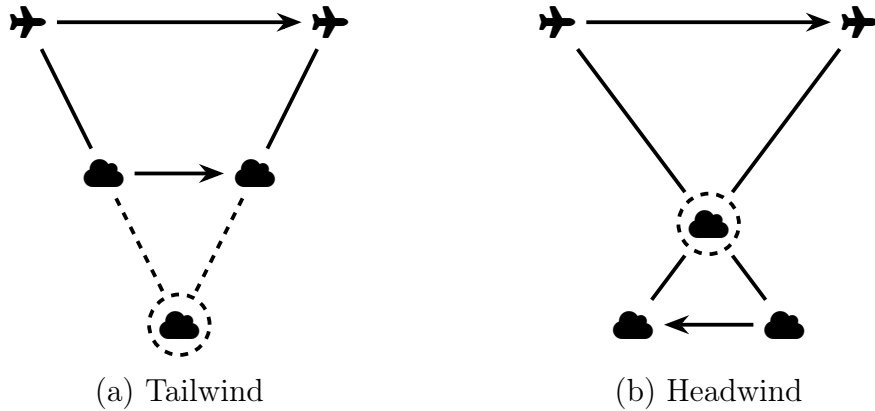


Figure 4: Causality of the position and height error resulting from disregarded (a) parallel and (b) antiparallel horizontal wind. In the case of tailwind (a), the intersection of the two viewing direction rays and thus the measured value is considerably lower than the moving cloud itself. Conversely, a headwind (b) leads to an overestimation of the cloud height. The sketch is not to scale.

the effect of the wind-cloud displacement. In Figure 4, two case studies illustrate the height and position error that would occur if the cloud drift is not taken into consideration. Deviations appear not only in the cases of parallel or antiparallel wind, but in any wind direction. However, the effect is very easy to observe in these instances.

The reconstruction relies on the fundamental assumption that the aircraft is moving faster than the measuring point. Compliance with this condition, however, is not a problem for the research aircraft in which VELOX was installed at a flight speed in the order of 200 m s^{-1} .

2.4.2 Overview of *Silver's* coordinate systems

For the technical implementation of the presented reconstruction scheme, it is necessary to switch between different coordinate systems. For instance, the position of the aircraft is given in coordinates of the World Geodetic System 1984 (WGS84). Later on, the cloud points should also be specified in this reference system. However, it is highly impractical to carry out calculations of Euclidean geometry in such an ellipsoidal system. Cartesian coordinates are preferable here. To achieve a comprehensible structure, it also makes sense to use several coordinate systems and describe their position relative to each other. VELOX, for example, has its own camera coordinate system defined within the aircraft reference system. As long as the aircraft position is known, it is possible to perform calculations directly in the camera system. This only requires determining the position and rotation of VELOX in relation to the aircraft's navigation system.

As a solution for this functionality, the mounttree package, developed by Kölling (2020), was chosen. It supports the conversion of position and direction vectors into geographical or Cartesian coordinates as well as the transformation into other coordinate systems. Typically, a main system with subsystems, each of which may also have subsystems, is used to define the coordinate systems. For *Silver*, the collection of

coordinate systems required for the reconstruction is set in the “velox.yaml” file. The basis is the earth reference system WGS84 in geographical coordinates. Within this, the aircraft reference system is defined by latitude, longitude, altitude and the roll-pitch-yaw angles. The values originate from the Basis HALO Measurement and Sensor System (BAHAMAS). The VELOX camera coordinate system is located relative to BAHAMAS. The positional parameters are obtained from technical drawings by enviscope GmbH, which was responsible for the development and certification of VELOX (Schäfer et al., 2022). The rotational values can slightly fluctuate from one campaign to the next due to removal and reinstallation and therefore should be checked and recalculated for each campaign on account of the high error impact on reconstruction data. How this can be done is described in more detail in Section 2.6.2. Additionally, in relation to the earth reference system, the stereo system is defined in which all computations of the reconstruction scheme are performed. The origin is located at the point P_{ref} shown in Figure 3, which lies exactly between the camera positions P_1 and P_2 at the two recording times. The location of this point is not affected by the wind correction. The coordinate axes x , y and z point in the north, east and nadir direction respectively. The first step of the reconstruction function, therefore, is to calculate the position of P_{ref} and use it to set up the stereo coordinate system.

2.4.3 Allocation of viewing directions

The cloud point pixels are then translated into viewing direction vectors within the camera system. This process requires a calibration file to be loaded, which assigns a viewing direction to each pixel, in this case in the form of a zenith and azimuth angle. The zenith angle describes the angle between the optical axis and the viewing direction of the pixel. The azimuth angle specifies the angle of rotation of the viewing direction in a mathematically positive system with the origin in flight direction. A description of the way in which the camera was calibrated is provided in Section 2.6.1. The calibration file contains the parameters for all pixels of the VELOX imager. If the brightness temperature dataset is trimmed at the edges, it is essential to correctly specify the parameter “vid_edge_trim”, which defines the number of pixels missing in the dataset in relation to the raw data at each edge. Otherwise, the corresponding viewing directions cannot be properly associated with the pixels.

Now the zenith and azimuth angles need to be assigned to each cloud point pixel. Doing this for the points in the first frame of the video is straightforward, as the Shi-Tomasi corner detection algorithm (Shi and Tomasi, 1994) returns integer pixels. However, after applying the optical flow algorithm (Lucas and Kanade, 1981; Bouguet, 2001), the cloud points usually no longer lie exactly on a camera pixel, but somewhere in between. This means that the angles must be linearly interpolated out of the four surrounding pixels. When interpolating, it is important to note that the azimuth angle is a circular variable, meaning there is a jump discontinuity. If the surrounding pixels are located on the transition boundary, the interpolation will be incorrect. This is similar to the case when calculating an arithmetic average from the almost northern compass bearings 1° and 359° . Mathematically, the result would be 180° , i.e. south, which makes no sense. This is not a problem with the zenith

angles, as they do not feature a similar jump discontinuity. In order to ensure that an azimuth angle can still be interpolated, the angles are transformed into sine and cosine values that do not exhibit a jump discontinuity. These values are interpolated separately and then converted back into an angle. Now that the two necessary angles are actually available for each cloud point pixel, the viewing direction vectors can be calculated within the camera reference frame.

For the sake of completeness, it must be mentioned that there are circumstances in which not all four surrounding pixels are present during an interpolation. This is only the case if the point tracked by the optical flow algorithm lies between the center of an edge pixel and the absolute edge of the image and the dataset trim of this side is zero. In such a case, the affected cloud point cannot be evaluated any further.

2.4.4 First reconstruction in calm air

Once the direction vectors have been obtained within the camera reference frame, they must be transferred to the stereo system for joint evaluation. Subsequently, the first cloud point reconstruction is performed. The first step is to check that the vector pairs are not collinear. Collinearity can occur if a bad-pixel is tracked instead of a cloud point. This refers to pixels that do not meet the accuracy requirements for measurement and do not move through the camera's field of view. Although a bad-pixel correction is carried out when processing the VELOX data (Schäfer et al., 2022), it can still occur, as the transition between good and bad pixels is fluent and the emergence is also temperature-dependent. After the check, the positions of the mis-pointing vectors as well as the cloud points are computed. Initially, calm air is assumed, as the position of the cloud point and thus the wind vector at said spot is not known yet. This condition provides a first estimate of the location.

2.4.5 Plausibility height filter

Characterized by their geographical position and altitude, the cloud points must be examined for plausibility. To do this, the derived heights are checked. Cloud points cannot be higher than the stereo reference system, as VELOX looks in the nadir direction and does not see above the horizon even when the research aircraft HALO is inclined. The height of the reference system corresponds approximately to the average altitude of HALO during the recording of the image pair. Furthermore, no cloud points are used that are below the height of the 1000 hPa layer according to the U.S. standard atmosphere (National Oceanic and Atmospheric Administration et al., 1976), i.e. below 110.8 m. In reality, such clouds can exist, but there is no reanalysis wind data available for them, which is essential for wind correction. The points are then checked again using a digital surface model. This ensures that no points lie below the ground or that the Earth's surface is incorrectly tracked. Points found less than 100 m above the ground are filtered out. If no or a spatially incomplete surface model is passed to *Silver*, sea level is assumed at the undefined positions, whereby the lowest points are removed by the 1000 hPa filter.

2.4.6 Iterative correction of the wind-cloud displacement

For the remaining cloud points, the wind correction is executed. This is performed iteratively, as the inclusion of the wind vector changes the initial position of the cloud point towards the corrected position. Because a different wind may prevail at the new position, the correction must be carried out again and repeatedly. *Silver's* default configuration uses five iteration steps to compensate for the wind-cloud displacement. This number has already proven to be a reasonable limit for Volkmer et al. (2024), as no significant improvements were achieved afterward.

Prior to a new reconstruction, however, the wind vector at the cloud point has to be evaluated first. For this purpose, data from the fifth generation European Centre for Medium-Range Weather Forecasts (ECMWF) atmospheric reanalysis (ERA5; Hersbach et al., 2020) is utilized. It provides a spatial resolution of $0.25^\circ \times 0.25^\circ$ on 37 pressure levels with a temporal resolution of one hour. Only the horizontal wind field is relevant for this, since convection is not sufficiently scaled. In order to link the pressure levels with the geographic heights of the cloud points, they are converted into each other assuming the U.S. standard atmosphere (National Oceanic and Atmospheric Administration et al., 1976). As the grid resolution for the individual points is still quite coarse, the wind vector is linearly interpolated to position and time. To do this, it is assumed that the dataset forms a rectilinear grid. The Earth does not quite fulfill this condition due to its ellipsoidal shape. However, the difference for the mesh size is usually quite small. Since the wind field also follows the curvature of the Earth, the interpolated values are likely to be more accurate than when converting and interpolating in a Cartesian coordinate system.

After the interpolation, the wind vector is applied in the reconstruction scheme of Figure 3, whereby a new position is calculated. Before the next iteration step commences, the plausibility of the heights is filtered again. At this point, however, the system only checks whether the points are located between the stereo reference height and the 1000 hPa pressure level. A repeated inclusion of the digital surface model is ineffective at this stage, as tracked ground points have already been removed. Of course, it is possible that ground points have been reconstructed too high due to measurement uncertainties and are consequently not filtered out. However, such points can no longer be distinguished from low clouds, regardless of the futility of wind correction for ground points. Hence, the points are granted appropriate freedom of movement during the correction. Only after running through all iteration steps is a final check made using the digital surface model to ensure that no points have fallen into the ground or the 100 m high containment layer.

It should be noted that the reanalysis dataset may also deviate from the true wind vector. Volkmer et al. (2024) gathered several studies that quantify uncertainties in different regions and altitudes. They found discrepancies of up to 3 m s^{-1} , which can lead to height errors of well over a hundred meters given typical values. Caution is advised when it comes to clouds formed, for instance, by Foehn winds or gravity waves, where the assumption that the clouds move with the horizontal wind does not usually hold true.

2.5 Resulting datasets

After a successful stereographic reconstruction of cloud points from the brightness temperatures measured by the VELOX imager, the resulting dataset is saved in the form of a NetCDF file. For each reconstruction step in which cloud points were calculated, the mean recording time of the image pair used for the reconstruction, the position of the stereo reference system and the positions of the cloud points in geographical coordinates of the WGS84 reference system are written to the drive. Since the number of reconstructed points per image pair can vary, the individual cloud point arrays are evenly filled with NaN values to obtain the same shape. The specified position of the stereo reference system's origin can be interpreted as the location of the measurement if later only one measuring location should be stated. Currently, no further distinction is made regarding why reconstructed data might not be available for a particular time step. Causes for this include gaps in the brightness temperature dataset, insufficient contrasts when calculating the optical flow or simply the non-existence of clouds. It is planned to implement a more detailed indication of this in the future, whereby gaps in the time axis will vanish.

2.6 Geometric camera calibration

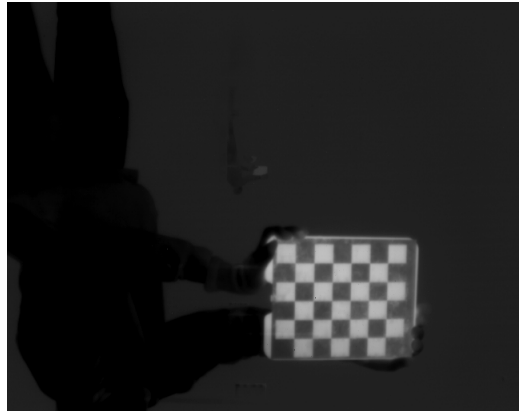
2.6.1 Pixel viewing direction in the camera system

In order for the images of a camera to be reconstructed stereographically, each pixel must be allocated a viewing direction. This is realized through camera resectioning, which typically entails photographing a chessboard from various directions. It simultaneously considers optical effects such as radial and tangential distortion. Compared to cameras that operate in the visible spectral wavelength range, thermal infrared cameras constitute a particular difficulty in the construction of a suitable chessboard target. It must succeed to combine two objects that radiate a different amount of energy in the thermal infrared spectrum to detect a pattern in the images.

A comparatively simple approach is the utilization of two materials with substantially different emissivities. For this case, a polished brass plate with low emissivity was chosen, onto which small paper squares featuring a high emissivity coefficient were attached. Assuming uniform material temperature, the brass plate should exhibit a significantly lower brightness temperature compared to the paper squares. The tradeoff is that, given the absence of transmittance, a material with low emissivity demonstrates high reflectance. The brass plate, therefore, reflects a large proportion of the ambient radiation into the camera. This is especially problematic when the camera sees itself. With such inhomogeneities in the chessboard images, it is almost impossible to perform a proper calibration. However, this can be remedied to some extent by deliberately cooling down the target, as proposed by Herrmann et al. (2019). As a result, both materials emit only little thermal infrared radiation. Their reflective properties are retained, however, causing the brass squares to reflect a lot of ambient radiation into the camera. In contrast, virtually no radiation of this kind is released by the paper squares. Because of this, the brass in the camera image stands out from the paper squares due to a higher brightness temperature. The cooling was achieved with the aid of a large ice pack.



(a) Ordinary camera



(b) VELOX imager

Figure 5: Appearance of the chessboard target in (a) the visual spectral range and in (b) thermal infrared. The contrast range of (b) was adapted to the value range of the brightness temperatures within the chessboard and is inverted, i.e. brighter hues indicate lower values.

Now a variety of chessboard images could be produced. In this process, it was important that the full camera field of view was covered with the differently oriented target. Figure 5 displays the constructed target as seen through an ordinary camera and by the VELOX imager. To achieve the best possible pattern recognition by the calibration algorithm, the contrast range of the images was adapted to the value range of the brightness temperatures within the chessboard. The next step consisted of finding suitable images for calibration. For this purpose, the images in which the algorithm did not detect a complete pattern were initially removed. Afterward, the images were checked for heterogeneity in order to cover the camera's field of view as evenly as possible. To do this, the position of the chessboard corners in an image was compared with the positions from the collection of images already approved for calibration. Only when the mean squared error (MSE) to each image equaled or exceeded 1000 px^2 , was the tested image also approved. This resulted in 42 good images with a total of 1260 corners (42 images \times 30 corners per image), shown in Figure 6. It is evident that the center of the field of view is well covered, yet the algorithm recognized only a limited number of images at the field of view's outer edges. This is an issue, though it can be attributed to the general calibration problems described at the end of this section.

The images were applied to the calibration algorithm provided by OpenCV (a). As the camera model, the default five-parameter model was selected, which compensates for radial distortion with three and tangential distortion with two coefficients. Based on this, the zenith and azimuth angle of the viewing direction could be calculated for each pixel. Different camera models were tested as well, but no significant improvements were found. When checking the calibration quality, the re-projection error was found to be 0.55 px. This measure describes the magnitude of the standard distance between a spatial point projected into the image plane by the camera model and the actual measured position in the image plane. It is computed like a root mean square error (RMSE) and should be as small as possible. The observed value appears

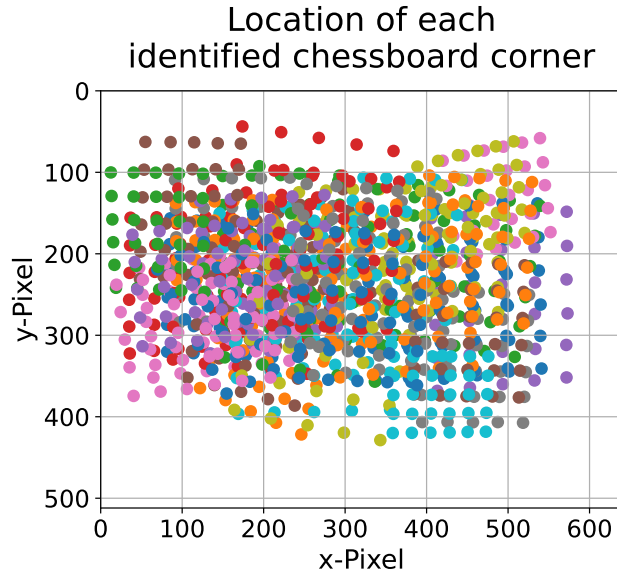


Figure 6: Position of all 1260 chessboard corners ($42 \text{ images} \times 30 \text{ corners per image}$) considered in the camera calibration, within the image plane. It shows the coverage of the camera’s field of view that could be achieved under the given circumstances, as well as slight signs of the not yet corrected distortions. Corners from the same image feature the same color. However, due to the large number of pictures, different images do not provide an unique color.

to be quite good according to the rules of thumb for camera calibration. Kölling et al. (2019) applied a modified form of the re-projection error and calculated it as the mean absolute error (MAE). The VELOX calibration scored 0.57 px in this case, but was still considerably undercut by specMACS with 0.15 px (Kölling et al., 2019). This raises the question of whether this is sufficient for such an error-sensitive application.

During the calibration, three main problems emerged, whose solution would significantly improve the results, but could not be addressed within the scope of this work. The first issue was the condensation of water vapor on the cooled target, which led to inhomogeneities in the chessboard pattern. Although it was wiped dry between measurements, the effect lasted only a short time. To solve this, the calibration would need to be performed in dry enough air to prevent condensation, which would require a suitably large climate chamber. A further idea might be to shield the chessboard with a thin infrared-permeable plate featuring a special superhydrophobic coating (Wahab et al., 2023). Eventually, it could be possible to dispense with cooling the target entirely, provided there is enough incoming infrared radiation from the environment. Specifically, this would imply a large warm wall behind the VELOX imager. However, this is not easily feasible either.

In addition to the irregularities caused by condensation, inhomogeneities also originate from disparities in the radiances of the thermal infrared radiation emitted by the ambient room and camera components. To counteract this, the ambient room should only contain objects with a uniform temperature and emissivity coefficient. The camera components need to be concealed to the extent possible with a uniform, room-like material.

The third problem concerns the target size. Since the imager's focus point is set to a large distance, close-ups of the chessboard appear blurred and are difficult for the algorithm to identify. Therefore, a distance to the camera of at least two meters should be maintained. Because of that, the chessboard ($0.28\text{ m} \times 0.24\text{ m}$) could only cover a small part of the image frame. This makes it all the more challenging for the algorithm to rectify those short lines. The only remedy here is a larger target, which is planned to be built in the future.

2.6.2 Position of the camera system in the aircraft system

Once the viewing directions have been calculated for all pixels of the camera system, it is necessary to be able to translate them into the aircraft reference system. To do this, it is required to determine the precise position of the VELOX imager in relation to BAHAMAS' navigation system. The positional parameters were straightforward to obtain and originate from the technical drawings of HALO. The rotational orientation had to be derived from a georeferenced image specifically for the HALO-(\mathcal{AC})³ campaign taken as a case study in this thesis.

Figure 7 shows the VELOX image used for this purpose. It is well suited as it exhibits numerous ground control points thanks to Bardufoss Airport (Norway) and the surrounding town. Furthermore, the visibility is not obscured by clouds.

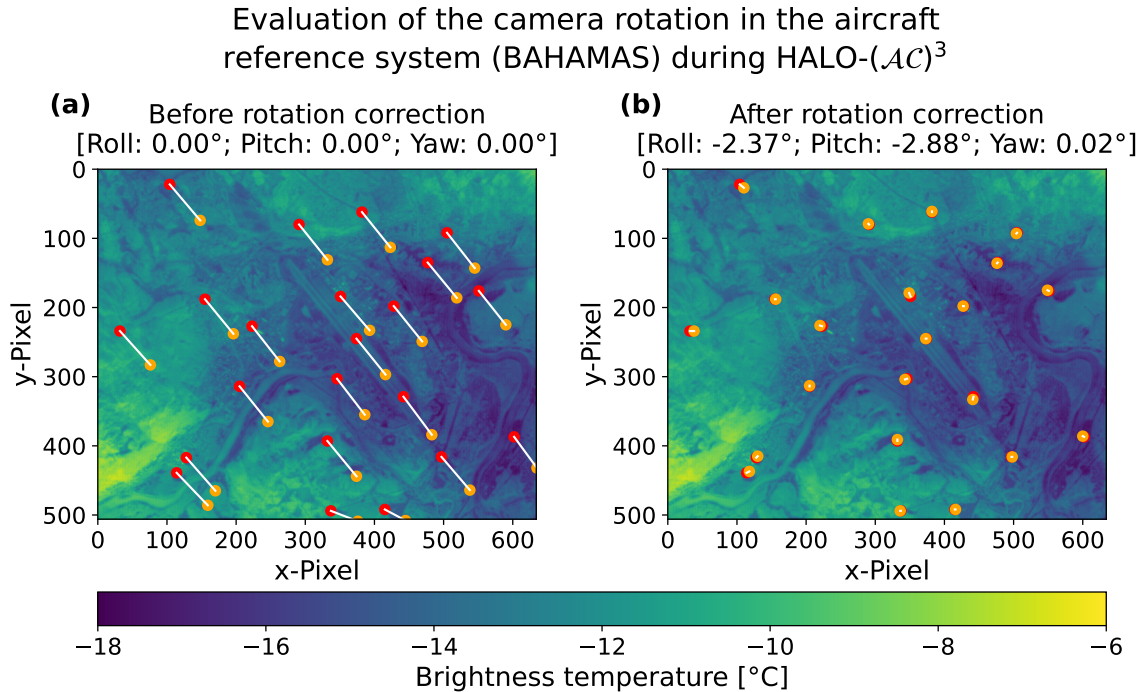


Figure 7: Correction of the rotational angle offset performed for the HALO-(\mathcal{AC})³ campaign. The georeferenced VELOX image was captured during flight RF03 at 2022-03-13T08:22:24Z over Bardufoss Airport (Norway). Ground control points are each marked with a red and orange dot for the measured and theoretical position. Theoretical positions outside the image cannot be properly projected into the frame, causing the misaligned connection lines at the bottom edge of panel (a).

The image was captured from an altitude of slightly more than 10 km, making it a little less sensitive to uncertainties when locating ground control points compared to images from low altitudes. For georeferencing the recognizable patterns visible in the image, the online services *Mapy* ([Seznam.cz](#)) and *Altimeter* ([Coordinates-converter.com](#)) were used. The dots marked red in Figure 7 depict the positions of the ground control points in the VELOX picture. The orange dots indicate the locations where the ground control points should actually be in the image according to the angle calculations. It can clearly be seen in Figure 7a that there are systematic deviations in the neutral position before the correction.

To fix this, angle combinations were methodically tested and the discrepancies calculated. As a measure of error, the RMSE from the angular deviations between the measured and calculated viewing directions was chosen. The combination of rotational angles that attained the smallest error was considered the optimum and used during the reconstructions. It was found at [Roll: -2.37° ; Pitch: -2.88° ; Yaw: 0.02°] with an error of 0.17° . The result of this correction can also be seen in Figure 7b. The points of measurement and calculation are now almost aligned. Deviations occur because of uncertainties in the georeferencing and an imperfect camera calibration.

3 Evaluation for test cases

To evaluate the expectable quality of the data reconstructed by *Silver*, five test cases were designed from the VELOX datasets collected during the HALO-(\mathcal{AC})³ campaign. This primarily involves the examination of altitude data, since these can be compared relatively well with other data sources and with themselves. They reveal problems most clearly, also because they tend to exhibit the greatest errors in the presence of imprecision. Simultaneously, it is possible to deduce the accuracy of the horizontal position if the height values are precise, as these values are coupled by the three-dimensionality of the matter.

3.1 Comparison between Lidar and *Silver*

The entry point into the test series is understandably a direct comparison with altitude data obtained via a different measurement method. Suitable datasets for this are those from the airborne multi-wavelength water vapor differential absorption lidar WALES (WAter vapor Lidar Experiment in Space; Wirth et al., 2009), which was also on board HALO during HALO-(\mathcal{AC})³. To use them and if not already available, the measured cloud top heights must be extracted from the backscatter ratio data, which was the case for HALO-(\mathcal{AC})³. This is accomplished by searching for the maximum height at which a threshold backscatter ratio is still exceeded. For the registration of cumuliform clouds, a backscatter ratio of 40 is appropriate due to the high optical thickness. If instead stratiform clouds are investigated, a value of 10 is sufficient, as the upper edges of these clouds are usually somewhat optically thinner.

The major difference to VELOX is that this active remote sensing instrument is only oriented towards nadir. To achieve comparability, the reconstructed cloud points,

therefore, must be selected in a controlled manner. For this purpose, a cylinder is defined around the beam of the lidar measurement. All stereo cloud points that were collected within a certain time (sampling time) around the lidar measurement and lie within this cylinder are used for the comparison. The cylinder was designed with a radius of 150 m. The reason for this is that the lidar data has a temporal resolution of 1 Hz and is averaged over this period. The distance traveled by the aircraft per second is in the order of 200 m. Consequently, the cylinder should also be in this order of magnitude.

Now two cloud types were analyzed in more detail. The first flight segment was conducted during research flight RF11 on 2022-03-30 and featured cumuliform cloud cover. In contrast, the leg flown on 2022-03-15 (RF05) showed stratiform cloud properties. A sampling time of ± 5 s was used in both scenarios, whereby the case of ± 1 s was also tested for RF11. The results are visualized in Figure 8. For each of the three investigated elements, the time series (Figure 8a, c, e) of the reconstructed cloud points including the lidar measurements and the equivalence (Figure 8b, d, f) of the data sources are shown.

It is evident that with a sampling time of only ± 1 s (Figure 8a, b), the leg featuring cumuliform cloud cover obviously reveals fewer cloud points than with ± 5 s (Figure 8c, d). However, these points follow the lidar time series (Figure 8a) well and thus also fall close to the equivalence line in the conformity plot (Figure 8b). The RMSE of 147 m is caused primarily by outlier values above the 1000 m height line. Neglecting these points yields an RMSE of 59 m, which indicates significant agreement. It is hard to determine what caused these artifacts. One possible reason is that there were indeed higher clouds within the cylinder that were not detected by the lidar. However, it is also conceivable that deviations were caused by turbulence, for example. In order to avoid such cases, Kölling et al. (2019) also filter by the length of the mis-pointing vector during the reconstruction. In *Silver*, this has not yet been implemented in order to obtain a preferably unadorned picture. In the future, the influence of such a filter on the reconstruction data will be investigated.

Looking at the same flight segment with a sampling time of ± 5 s (Figure 8c, d), it can be observed that the points still follow the lidar data, but that there is an increasing systematic overestimation of the cloud heights. Likewise, the RMSE increases to 179 m. As will be shown in more detail in the next test cases, this is caused by an inadequate viewing direction calibration that does not properly consider radial distortion. As a consequence, the heights of cloud points are overestimated the further away they are from the optical center of the image.

The stratiform flight leg (Figure 8e, f) presents a predictable image. Practically no cloud points are reconstructed here and those that are found are too heavily erroneous, with an RMSE of 2591 m, to be used in any meaningful way. The reason for this lies in the methodology itself, as it requires sufficient contrasts on the cloud surfaces, as explained in Section 2.3.2. For homogeneous stratiform clouds, this is simply not given. It is therefore advisable to develop a technique to avoid reconstructing such scenarios in order to maintain data quality. In these cases, the cloud heights can be derived from the brightness temperatures themselves, as the temperature profiles are rather consistent, lowering the uncertainties.

Comparison between Lidar and *Silver*

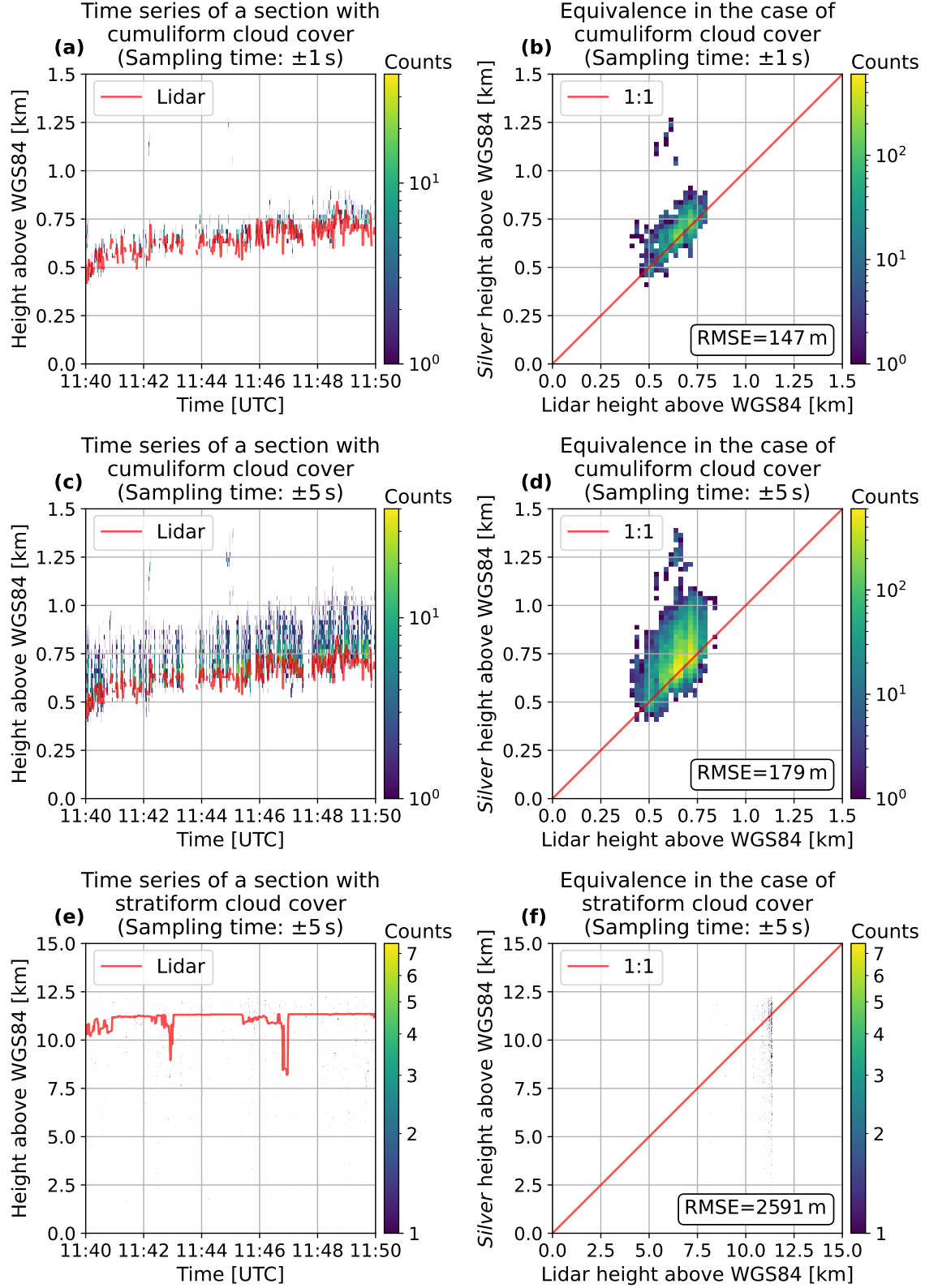


Figure 8: Comparison of reconstructed VELOX cloud heights with lidar data from WALES for different cloud types and sampling times. The cumuliform segment is from 2022-03-30 (RF11); the stratiform section was overflown on 2022-03-15 (RF05). For each case, the time series (a, c, e) and conformity plot (b, d, f) with the occurred counts are displayed. Please note that the scale may vary between individual plots due to the high count differences.

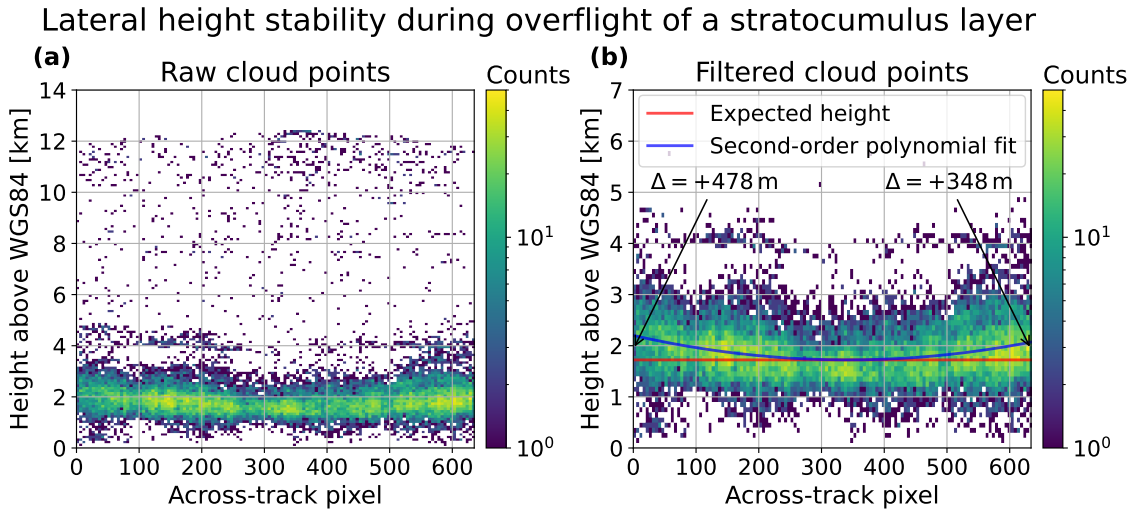


Figure 9: Investigation of the lateral height stability for a flight leg on 2022-03-15 (RF05) between 09:54:00Z and 09:58:00Z, during which stratocumulus clouds were overflown. Presented are the cloud heights as a function of their across-track pixel position within the VELOX image. A distinction is made between (a) raw data and (b) filtered points that have traveled a Euclidean distance of less than 25 px across the image pair. For these data, a regression with a second-order polynomial has been conducted and the actual expected cloud height has been plotted.

3.2 Lateral height stability

The next test examines the lateral stability of the reconstructed points. In other words, it is checked whether the quality of cloud points changes depending on where they are located in the VELOX image pair. It is especially important to look at the development along the transverse axis of the aircraft, as clouds located at these image edges are not directly overflown at a different point in time. For an analysis, a stratocumulus cloud field is required, as this provides contrasts that are indispensable for a reconstruction, while simultaneously permitting the assumption of a constant altitude, even if this is interrupted by small variations. A suitable cloud field could be found during flight RF05 on 2022-03-15 between 09:54:00Z and 09:58:00Z. For a point reconstructed during this flight leg, it was possible to calculate a mean pixel position from the positions in the image pair.

This was done for all cloud points and plotted in Figure 9. Here the height values are compared with the across-track pixel position. When looking at the raw data (Figure 9a), the position of the stratocumulus layer is clearly recognizable. However, there are also numerous stray points that do not really fit into the scene. These emerge when the measurement signal is low and the value range is comparatively narrow, like in this case, rendering small inhomogeneities in the measurement apparatus much more visible, which are then mistakenly tracked by the algorithm. The VELOX imager operates with a filter wheel rotating at 100 Hz, which incorporates six filters used to measure five different spectral channels (Schäfer et al., 2022). These filters are designed to have a plane surface. However, it is technically impossible to produce them absolutely flat. Small deviations are reflected in the thickness and shape,

affecting the interaction with thermal radiation by causing inhomogeneities. The inhomogeneities of the installed filters are small, but become noticeable under such circumstances as horizontal stripes in the images.

Since these stray points must be removed for a statistical assessment, it was stipulated that the Euclidean distance between the pixel position in the first and second image must be less than 25 px. The result is presented in Figure 9b. Here it becomes clear what was already foreshadowed in Figure 8. With increasing distance from the optical center, the average height values deviate upwards, which does not correspond to the assumption of altitude constancy. For quantification, a second-order polynomial regression was performed, which covers effects due to imperfect correction of radial and tangential distortion. The expected height is the minimum of this fit, as it matches the spot already checked by the WALES lidar and found to agree well. Over the time period, no cloud top height lidar data was available for a direct comparison. This results in an average deviation of +478 m on the port and +348 m on the starboard side, whereby the discrepancy between the two values is primarily caused by the offset between the image center and the optical center.

The findings reveal an undercorrection of radial distortion and suggest that reconstructions with this camera calibration should only be used with caution. Before entire flights are actually processed, a new viewing direction calibration must be created according to the solutions formulated in Section 2.6.1.

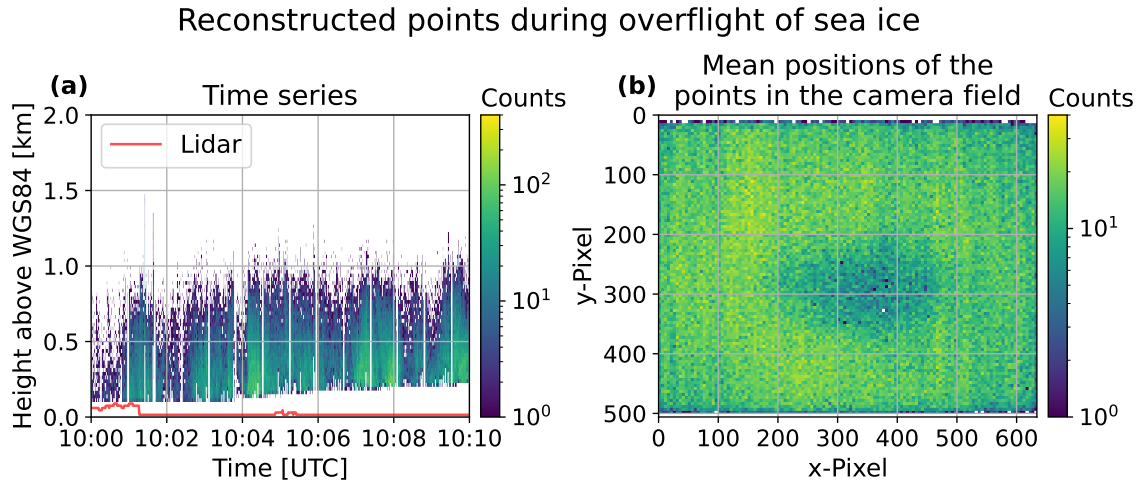


Figure 10: Check whether ground points can be misinterpreted as cloud points. For this purpose, a cloudless sea ice surface was overflowed on 2022-03-30 (RF11) between 10:00:00Z and 10:10:00Z. Shown are (a) the time series of the reconstructed ground points including the lidar measurements by WALES as well as (b) the origin locations within the camera image. Please note that the scale varies between the time series and the origin location analysis due to the high count differences.

3.3 Behavior for visible ground

The following test case focuses on the handling of ground points. For this purpose, a section between 10:00:00Z and 10:10:00Z was chosen from flight RF11 on 2022-03-30, which only featured contrast-rich sea ice without the presence of clouds. Ideally, no points should be reconstructed because the height filter described in Section 2.4.5 eliminates ground values.

Figure 10 presents the time series of the reconstructed points (Figure 10a) as well as the mean positions in the camera image from which the detected points originate (Figure 10b). It is evident from Figure 10a that, despite the theoretical absence, points were identified that are up to 1000 m above the ground. That can be explained by the insufficient camera calibration and the subsequent application of the wind correction to ground points. This reasoning is supported by Figure 10b, the origin analysis of the cloud points in the camera field. Here it becomes apparent that the fewest points originate from the area of the optical center, where the calibration is most accurate. Instead, the majority of points originate from the image edges, which are most affected by the optical distortion and are notorious for height overestimation.

It can therefore be concluded that the current camera calibration can cause the misinterpretation of ground points as cloud points. This particularly affects the image edges, but even the optical center can occasionally generate these points due to measurement uncertainties. At the present time, the only way to prevent this is to expand the containment layer from Section 2.4.5 or to limit the use to points emanating from the optical center.

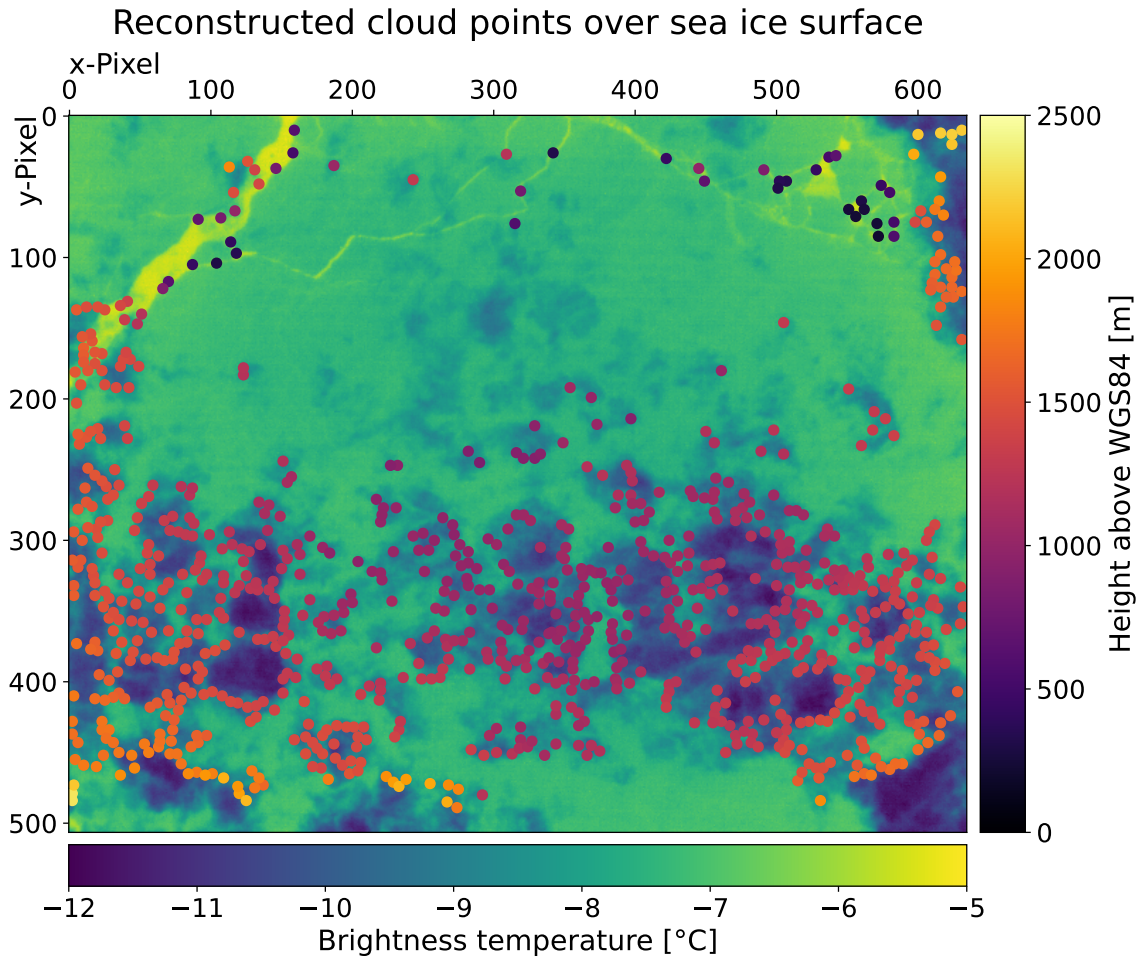


Figure 11: *Silver* generated data product using the example of cumulus clouds over a sea ice surface. The depicted brightness temperatures were captured at the time 2022-03-16T15:57:20Z (RF06). Marked are all reconstructed cloud points and their color-coded heights, which were derived from the combination of this and the temporally next image. It demonstrates that despite the lack of visual contrasts, a reconstruction in the thermal infrared remains possible.

3.4 Low contrasts in the visible spectrum

The final test scenario summarizes the potential offered by stereographic reconstruction of brightness temperatures via *Silver*. To this end, the case of scattered cumulus clouds over a sea ice surface was studied in more detail. For cameras operating in the visible spectrum, such an event poses a serious problem, since the bright clouds are barely distinguishable from the bright sea ice surface. The associated lack of contrast allows only sparse evaluation. This problem disappears in the thermal infrared range, because clouds and the ground usually feature dissimilar temperatures and thus disparate radiances. The consequence are clouds that are well separable from the ground, as shown in Figure 11.

This measurement was taken at 2022-03-16T15:57:20Z during flight RF06. It additionally contains all reconstructed points that were derived by processing the combination of this and the temporally next image. These points exhibit a rather

uniform height in the image center that increases towards the image edges owing to the camera calibration. In the upper part of the image, isolated ground points can be spotted. It becomes noticeable that the identified cloud points are located at the cloud boundaries with the strongest contrasts and hit these despite the imprecise calibration. But this is due to the fact that the same viewing direction calibration was utilized for the back-transformation into pixel coordinates, which is why the distortions approximately cancel each other out.

The above case is representative for all instances of poor visual contrasts. *Silver* thus enables the stereographic reconstruction of night flights as well.

4 Case study on cloud height progression during a cloud streets event

With all quality checks completed, a first case study has been conducted on a phenomenon which constituted one research focus of the HALO-(\mathcal{AC})³ campaign. This concerns cloud streets, i.e. organized, almost parallel running rows of clouds within the convective boundary layer (CBL). In the Arctic, they are a common occurrence and can be well observed through satellite images. Cloud streets form in this region during cold air outbreaks (CAO), whereby cold, dry air pushes southwards, leaving the closed ice surface and passes over warm seawater. This leads to a strong air mass transformation, which is characterized by a rise in air temperature and humidity as well as labilization. Gryscha et al. (2014) explain that thermal instability in combination with vertical wind shear is the trigger for the secondary circulation that creates the cloud streets.

An important measure to gauge the extent of this phenomenon is the stability parameter $\zeta = -z_i/L$, where L denotes the Monin-Obukhov length and z_i the CBL height. This parameter can be interpreted as a normalized ratio between buoyant and shear production of turbulent kinetic energy, i.e. smaller values indicate a greater importance of wind shear in the CBL and vice versa. Gryscha et al. (2008) distinguish between two types of cloud streets based on their genesis. “Free rolls” are self-organized structures that can emerge at $\zeta < 20$. “Forced rolls” are induced by heterogeneities in surface temperature, such as caused by broken sea ice. The latter are spatially much more pronounced and can also occur at $\zeta > 20$. However, if ζ becomes too large, roll convection is superseded by cellular convection.

Gryscha et al. (2014) demonstrated this effect in large-eddy simulations (LES), showing that the stability parameter increases with increasing distance to the ice edge. It also exhibited the transition from roll to cellular convection. This is accompanied by an increase in the CBL height and a rising inversion base due to the persistent strong heat flux over the seawater, as evidenced by the simulations of Gryscha et al. (2014). This effect is visible through ascending cloud heights, which can be analyzed via *Silver*.

For this purpose, a leg of the HALO-(\mathcal{AC})³ flight RF13 dated 2022-04-04 and captured between 13:12:30Z and 13:19:00Z was examined. During this period, a structure of cloud streets was transversely overflowed, as shown in the satellite composite image in Figure 12a. The orange arrow marks the flight course. Although the flight track

Evolution of the cloud and CBL height during overflight of cloud streets

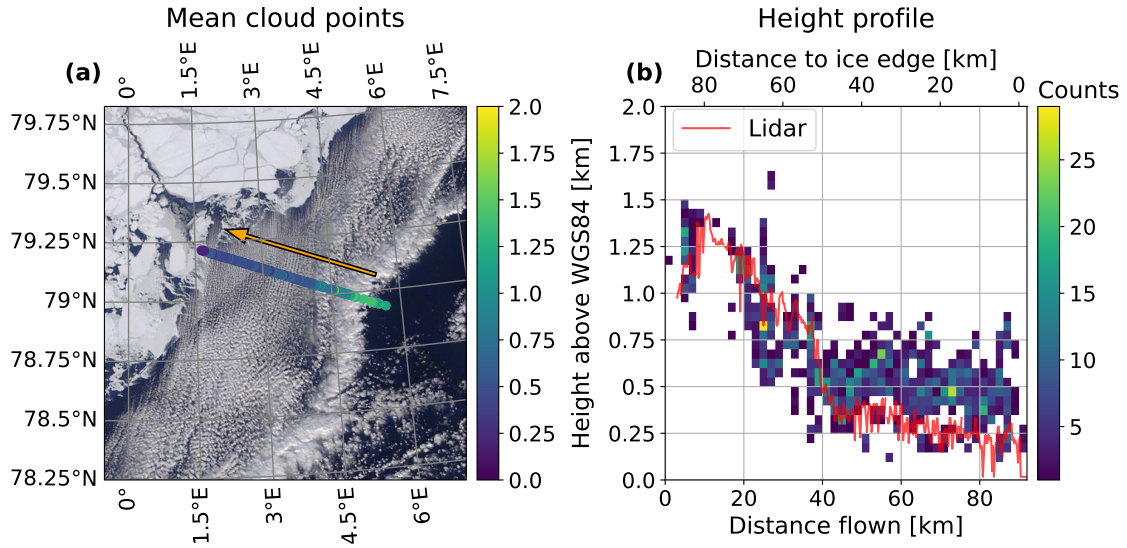


Figure 12: Cloud height development and associated extent of the convective boundary layer (CBL) during a cloud streets event on 2022-04-04 (RF13). The flight segment covered a distance of 92 km crossing the cloud streets between 13:12:30Z and 13:19:00Z. The cloud structures are clearly visible in the true-color satellite composite image (a), captured by MODIS (National Aeronautics and Space Administration Worldview, 2022). Marked therein are the cloud points averaged per measurement period, whose heights are color-coded. They indicate the flight track. The orange arrow shows the aircraft course. Plot (b) presents the altitude profile with the occurred counts of the considered cloud points depending on the flown distance and distance to the ice edge. Included are also the cloud top heights, obtained with the WALES Lidar.

is rather transverse to the development of the individual cloud streets, due to the position of the ice edge, clouds that were measured first have nevertheless traveled a greater distance over the open ocean. Therefore, a cloud height reduction should also be observable with increasing distance flown when approaching the ice edge. The investigation joins the study by Klingebiel et al. (2025), which analyzes exactly the same event, whereby one focus was set on the investigation of the microphysical properties of these clouds.

For the analysis of the reconstructed points, a cylinder of radius 150 m was defined around the aircraft's almost nadir-directed yaw axis at the time of measurement in compliance with the lidar comparison from Section 3.1. All points located in the cylinder during a sampling time of ± 1 s were selected, as these cloud points already showed significant agreement during the lidar comparison.

Figure 12 presents the results. In Figure 12a, all points considered per measurement time are combined into an average point, color-coded to visualize the height development. The picture corresponds to the expectations, since the cloud height and thus the CBL altitude decreases when approaching the ice edge. The progression can be seen even more detailed in Figure 12b, which depicts the heights of all considered

points as a function of the distance flown and the distance to the ice edge. The illustration also reveals that the cloud height is lower if the air mass has spent less time above the open sea surface, based on the knowledge that in this case the dwell time is positively correlated with the distance to the ice edge. The altitude gradient is particularly strong in the initial 40 km of the flight track, which is because the air masses there exhibit strong differences in the dwell times above the open sea surface as a result of the wind field and position of the ice edge. This can also be discerned in Figure 12a, where this area already shows cellular convection. After passing this mark, there is a rapid change to roll convection.

An interesting effect becomes clear when displaying the lidar cloud top heights as well, which were derived from the backscatter ratios as described in Section 3.1. In the region of the still young, thin cloud streets, these values are in the lower range of the reconstructed points. This effect could be due to the different measured spectra and the averaging of the backscatter ratio over the measurement period. However, it is also conceivable that significant deviations from the assumed ERA5 wind field arise due to the secondary circulation, which impairs the wind correction. Though this could also be seen as an opportunity to gain an impression of the prevailing wind field.

5 Conclusions

Within the scope of this thesis, the program for Stereographic Infrared reconstruction of cLoud points with the airborne VELOX imagER (*Silver*) was developed and documented. The objective was to retrieve the three-dimensional position of points on cloud structures via stereography utilizing the parallax resulting from the movement of an aircraft. In this context, brightness temperature datasets collected with the nadir-directed, airborne VELOX imager constituted the data foundation. This imager is frequently installed on board the High Altitude and LOng Range Research Aircraft (HALO) and forms a component of the passive remote sensing instrument VELOX (Video airbornE Longwave Observations within siX channels; Schäfer et al., 2022).

The program operations were presented, including the video generation, the identification and tracking of contrast-rich image points, the coordinate systems required for the computations and the reconstruction of the cloud points (Kölling et al., 2019), including a wind correction based on reanalysis data (Volkmer et al., 2024). Behind the wind correction stands the assumption that the clouds displace with the horizontal wind field. Convection or special cases, like rather stationary clouds formed by Foehn winds or gravity waves, cannot be taken into consideration.

For the functionality, a geometric camera calibration for the imager was necessary. This involved the construction of a chessboard target visible in the thermal infrared spectrum, which was used to generate numerous calibration images that were applied to a camera model. This allowed the allocation of a viewing direction in the camera reference system to each camera pixel. In order to convert these viewing directions into the aircraft reference system, the position and rotation of the imager in relation to the aircraft navigation system was ascertained with the aid of technical drawings and an image georeferencing.

To evaluate the processing quality, five test cases were designed from the datasets collected during the HALO-(*AC*)³ campaign (Arctic Amplification: Climate Relevant Atmospheric and Surface Processes, and Feedback Mechanisms). These comprised flight legs over cumuliform and stratiform clouds, a stratocumulus layer, sea ice and cumulus clouds over sea ice. It was found that cumuliform clouds can be very well detected due to the high contrasts present in these images. In comparison with lidar measurements, a root mean square error (RMSE) of 147 m was achieved in the test case, which dropped to 59 m after stripping outliers. Data acquisition for highly homogeneous stratiform clouds is much more difficult and should be entirely avoided beyond a certain degree in order not to jeopardize the general quality of the dataset. Additionally, it has become clear that it's no use carrying out more than just tests with the currently available viewing direction calibration. This was expressed at the image edges by overestimated altitude values of up to +500 m and through the misinterpretation of ground points as cloud points.

For a future scientific assessment of flights, it is therefore essential to develop an improved camera calibration. To do this, the chessboard target must be enlarged and inhomogeneities due to condensation and deviating ambient radiances suppressed. Consequently, the rotational angle offsets must be corrected too. *Silver* itself can be further optimized as well. This includes the installation of filters that consider the effects of turbulence and inhomogeneities within the camera apparatus, the specification of reasons for data gaps and the acceleration of processing. Subsequently, further flights and conditions will be tested and compared with other instruments in order to determine the uncertainties.

Although it is not yet possible to provide an exact error estimation due to a lack of precise calibration, the comparison with lidar measurements indicates that a height RMSE of less than 100 m appears possible. In a case study on a cloud streets event, the characteristic decline in cloud height and thus the convective boundary layer (CBL) when approaching the ice edge could already be observed within this thesis.

Silver, therefore, closes the data gap that occurs through insufficient contrasts in the visual spectral range. This affects cases such as clouds over an ice or snow surface and fairly obvious night flights. The data can then be used to investigate the extent to which other products can be derived from it. Conceivable examples include spatially mapped cloud masks or the three-dimensional rendering of cloud structures, although this could pose a challenge due to the VELOX imager's limited field of view.

Appendix A: Setting up *Silver*

The following section describes how to install and configure *Silver* in order to perform your own reconstruction. A running Python distribution is a mandatory requirement. The first step is to clone the *Silver* repository ( - Rothenberg, 2025). Alternatively, the files:

▷ silver.py	Contains the main program
▷ silver_lib.py	Provides the set of all functions required for reconstruction
▷ namelist.py	Configuration file
▷ velox.yaml	Defines utilized coordinate systems
▷ Velox-VDC.nc	Viewing direction calibration of the VELOX imager

can be downloaded individually. The “Sample” folder contains a demo dataset for testing the installation. Necessary dependencies:

▷ pathlib	Part of The Python Standard Library
▷ os	Part of The Python Standard Library
▷ multiprocessing	Part of The Python Standard Library
▷ xarray	
▷ rioxarray	
▷ opencv	(cv2)
▷ numpy	
▷ mounttree	
▷ metpy	
▷ scipy	

must be installed. The usage of a Conda environment is recommended.

Now the configuration file “namelist.py” should be opened to adjust the parameters for the upcoming reconstruction. The parameter “Velox_BT_File” is given the path to the VELOX brightness temperature dataset. This data must comply with the format of the published Halo-(\mathcal{AC})³ datasets (Schäfer et al., 2023), as *Silver* is currently adapted to these. The VELOX imager provides data for five different spectral channels (Schäfer et al., 2022). Channel 1, also termed BT1 in the datasets, is generally recommended for reconstruction, as it offers the largest spectral scope with the highest signal-to-noise ratio and therefore greater contrasts. The second parameter “Velox_VDC_File” specifies the location of the VELOX imager’s viewing direction calibration. Next, the “HALO_IRS_File” must be set, containing the aircraft position data from the BAHAMA System (German Aerospace Center, 2022) with a time resolution of one second. By default, this dataset arrives with a time resolution of 10 Hz, which can also be used, but requires more storage. “MNT_File” indicates the location of the definition file for the coordinate systems used. The parameter “vid_edge_trim” specifies, as already mentioned in Sections 2.2 and 2.4.3, the number of pixels missing at each edge in the dataset in relation to the raw data. For the published Halo-(\mathcal{AC})³ data (Schäfer et al., 2023), this parameter reads [2, 1, 3, 4], whereby the numbers represent [Bow, Starboard, Stern, Port] of the camera field. The storage location of the ERA5 wind field (Hersbach et al., 2023) is set under “ERA5_UV_Wind_File”. The area covered by this dataset arises from

the overflowed area and should be selected generously to ensure that no cloud point lies outside the given wind field. All that is needed is the horizontal wind field with a temporal resolution of one hour on all pressure levels from 1000 hPa to the next pressure level after passing the maximum flight altitude, although it does not take much storage to download the higher pressure levels as well. This dataset must be in NetCDF format. The “DSM_file” parameter holds the path to the digital surface model (DSM), available as GeoTIFF. As a source, the Copernicus GLO-30 Digital Elevation Model (European Space Agency et al., 2024) is recommended, which is currently one of the best globally available models. Other datasets can also be used as long as they feature the same structure. For this parameter, it is possible to enter an empty string if no DSM should be applied to filter the cloud points. In addition, it is possible to cover only a partial area with the altitude data. This is necessary if a flight segment runs over the ocean, where data is usually not available. For cloud points outside the area covered by the DSM, sea level is assumed for the surface elevation. The save location for the reconstructed cloud points is set by “Pcs_save_path”. The penultimate parameter “process_number” defines the maximum number of parallel running reconstructions. *Silver* is equipped with a simple process parallelization, which enables the evaluation of several image pair videos simultaneously. Additionally, the datasets required during the reconstruction are loaded into the Random-Access Memory (RAM) in order to access them more quickly. If this work should be done on a system where this resource is not sufficiently available for the data, the last parameter “low_RAM” can be set to True.

Finally, the main program “silver.py” can be executed for the stereo processing. Depending on the computer system and the amount of cloud points tracked, it can take up to 30 min to process one minute of flight time. Even the increase of the “process_number” will not do much to change this. The exact bottleneck is not known yet and may lie somewhere in the interplay between CPU-bound and I/O-bound tasks. This obstacle should be reduced in the future, which will also be achieved by replacing the remaining for-loops, which are well readable but slow in Python, with array operations.

References

- Bouguet, J.-Y.: Pyramidal Implementation of the Affine Lucas Kanade Feature Tracker Description of the algorithm, Intel corporation, Microprocessor Research Labs, 5, 4, URL https://robots.stanford.edu/cs223b04/algo_affine_tracking.pdf, 2001.
- Bradski, G.: The OpenCV Library, Dr. Dobb's Journal of Software Tools, 2000.
- Coordinates-converter.com: Altimeter: location or current altitude, URL <https://coordinates-converter.com/en/altimeter>, 2025-04-13.
- European Space Agency, German Aerospace Center, and Airbus Defence and Space: Copernicus GLO-30 Digital Elevation Model, doi:10.5069/G9028PQB, URL <https://portal.opentopography.org/raster?opentopoID=OTSDEM.032021.4326.3>, 2024, 2025-04-21.
- Ewald, F., Kölling, T., Baumgartner, A., Zinner, T., and Mayer, B.: Design and characterization of specMACS, a multipurpose hyperspectral cloud and sky imager, Atmospheric Measurement Techniques, 9, 2015–2042, doi:10.5194/amt-9-2015-2016, URL <https://amt.copernicus.org/articles/9/2015/2016/>, 2016.
- German Aerospace Center: Mission: HALO-(AC)³ – HALO Database – The High Altitude and LOng Range Research Aircraft Database, doi:10.17616/R39Q0T, URL <https://halo-db.pa.op.dlr.de/mission/130>, 2022.
- Gryschka, M., Drüe, C., Etling, D., and Raasch, S.: On the influence of sea-ice inhomogeneities onto roll convection in cold-air outbreaks, Geophysical Research Letters, 35, doi:10.1029/2008GL035845, URL <https://onlinelibrary.wiley.com/doi/abs/10.1029/2008GL035845>, 2008.
- Gryschka, M., Fricke, J., and Raasch, S.: On the impact of forced roll convection on vertical turbulent transport in cold air outbreaks, Journal of Geophysical Research: Atmospheres, 119, 12,513–12,532, doi:10.1002/2014JD022160, URL <https://onlinelibrary.wiley.com/doi/abs/10.1002/2014JD022160>, 2014.
- Herrmann, T., Migniot, C., and Aubreton, O.: Thermal camera calibration with cooled down chessboard, in: Quantitative InfraRed Thermography Conference, Mulhouse, France, URL <https://hal.science/hal-03275440>, 2019.
- Hersbach, H., Bell, B., Berrisford, P., Hirahara, S., Horányi, A., Muñoz-Sabater, J., Nicolas, J., Peubey, C., Raluca Radu, Schepers, D., Simmons, A., Soci, C., Abdalla, S., Abellán, X., Balsamo, G., Bechtold, P., Biavati, G., Bidlot, J., Bonavita, M., De Chiara, G., Dahlgren, P., Dee, D., Diamantakis, M., Dragani, R., Flemming, J., Forbes, R., Fuentes, M., Geer, A., Haimberger, L., Healy, S., Hogan, R. J., Hólm, E., Janisková, M., Keeley, S., Laloyaux, P., Lopez, P., Lupu, C., Radnoti, G., de Rosnay, P., Rozum, I., Vamborg, F., Villaume, S., and Thépaut, J.-N.: The ERA5 global reanalysis, Quarterly Journal of the Royal Meteorological Society, 146, 1999–2049, doi:10.1002/qj.3803, URL <https://onlinelibrary.wiley.com/doi/abs/10.1002/qj.3803>, 2020.

Hersbach, H., Bell, B., Berrisford, P., Biavati, G., Horányi, A., Muñoz-Sabater, J., Nicolas, J., Peubey, C., Radu, R., Rozum, I., Schepers, D., Simmons, A., Soci, C., Dee, D., and Thépaut, J.-N.: ERA5 hourly data on pressure levels from 1940 to present, doi:10.24381/cds.bd0915c6, URL <https://cds.climate.copernicus.eu/datasets/reanalysis-era5-pressure-levels>, 2023, 2025-04-21.

Klingebiel, M., Ehrlich, A., Gryscha, M., Risse, N., Maherndl, N., Schirmacher, I., Rosenburg, S., Hörnig, S., Moser, M., Jäkel, E., Schäfer, M., Deneke, H., Mech, M., Voigt, C., and Wendisch, M.: Airborne observations of cloud properties during their evolution from organized streets to isotropic cloud structures along an Arctic cold air outbreak, EGUsphere, pp. 1–23, doi:10.5194/egusphere-2025-201, URL <https://egusphere.copernicus.org/preprints/2025/egusphere-2025-201/>, 2025.

Kölling, T.: Cloud Geometry for Passive Remote Sensing, Ph.D. thesis, Ludwig-Maximilians-Universität München, Munich, URL <https://edoc.ub.uni-muenchen.de/26161/>, 2020.

Kölling, T., Zinner, T., and Mayer, B.: Aircraft-based stereographic reconstruction of 3-D cloud geometry, Atmospheric Measurement Techniques, 12, 1155–1166, doi:10.5194/amt-12-1155-2019, URL <https://amt.copernicus.org/articles/12/1155/2019/>, 2019.

Lucas, B. D. and Kanade, T.: An Iterative Image Registration Technique with an Application to Stereo Vision, in: IJCAI'81: 7th international joint conference on Artificial intelligence, vol. 2, pp. 674–679, URL <https://hal.science/hal-03697340/>, 1981.

National Aeronautics and Space Administration Worldview: Corrected Reflectance (True Color) Terra/MODIS, URL <https://go.nasa.gov/3HM3kgM>, 2022, 2025-06-14.

National Oceanic and Atmospheric Administration, National Aeronautics and Space Administration, and United States Air Force: U.S. STANDARD ATMOSPHERE, 1976, Technical Memorandum NOAA-S/T-76-1562, National Oceanic and Atmospheric Administration, Washington, D.C., URL <https://ntrs.nasa.gov/citations/19770009539>, 1976.

OpenCV - Open Source Computer Vision: Camera Calibration, URL https://docs.opencv.org/4.x/dc/dbb/tutorial_py_calibration.html, a, 2025-04-13.

OpenCV - Open Source Computer Vision: Optical Flow, URL https://docs.opencv.org/4.10.0/d4/dee/tutorial_optical_flow.html, b, 2024-11-11.

Rothenberg, P.: *Silver* - The program for Stereographic Infrared reconstruction of cLOUD points with the airborne VELOX imagER, Leipzig Institute for Meteorology, URL <https://github.com/Paul-Rothenberg/Silver>, 2025.

Schäfer, M., Wolf, K., Ehrlich, A., Hallbauer, C., Jäkel, E., Jansen, F., Luebke, A. E., Müller, J., Thoböll, J., Röschenthaler, T., Stevens, B., and Wendisch, M.: VELOX – a new thermal infrared imager for airborne remote sensing of cloud and surface properties, *Atmospheric Measurement Techniques*, 15, 1491–1509, doi:10.5194/amt-15-1491-2022, URL <https://amt.copernicus.org/articles/15/1491/2022/>, 2022.

Schäfer, M., Rosenburg, S., Ehrlich, A., Röttenbacher, J., and Wendisch, M.: Two-dimensional cloud-top and surface brightness temperature at spectral band BT1 (7.7 to 12.0 μm) with 1 Hz temporal resolution derived at flight altitude from VELOX during the HALO-(\mathcal{AC})³ field campaign, doi:10.1594/PANGAEA.963378, URL <https://doi.org/10.1594/PANGAEA.963378>, 2023.

Seznam.cz: Mapy.com, URL <https://mapy.com>, 2025-04-13.

Shi, J. and Tomasi, C.: Good features to track, in: 1994 Proceedings of IEEE Conference on Computer Vision and Pattern Recognition, pp. 593–600, Institute of Electrical and Electronics Engineers, Seattle, WA, USA, doi:10.1109/CVPR.1994.323794, URL <https://ieeexplore.ieee.org/document/323794>, 1994.

Volkmer, L., Kölling, T., Zinner, T., and Mayer, B.: Consideration of the cloud motion for aircraft-based stereographically derived cloud geometry and cloud top heights, *Atmospheric Measurement Techniques*, 17, 6807–6817, doi:10.5194/amt-17-6807-2024, URL <https://amt.copernicus.org/articles/17/6807/2024/>, 2024.

Wahab, I. F., Bushroa, A. R., Wee Teck, S., Azmi, T. T., Ibrahim, M. Z., and Lee, J. W.: Fundamentals of antifogging strategies, coating techniques and properties of inorganic materials; a comprehensive review, *Journal of Materials Research and Technology*, 23, 687–714, doi:10.1016/j.jmrt.2023.01.015, URL <https://www.sciencedirect.com/science/article/pii/S2238785423000157>, 2023.

Weber, A., Kölling, T., Pörtge, V., Baumgartner, A., Rammeloo, C., Zinner, T., and Mayer, B.: Polarization upgrade of specMACS: calibration and characterization of the 2D RGB polarization-resolving cameras, *Atmospheric Measurement Techniques*, 17, 1419–1439, doi:10.5194/amt-17-1419-2024, URL <https://amt.copernicus.org/articles/17/1419/2024/>, 2024.

Wirth, M., Fix, A., Mahnke, P., Schwarzer, H., Schrandt, F., and Ehret, G.: The airborne multi-wavelength water vapor differential absorption lidar WALES: system design and performance, *Applied Physics B*, 96, 201–213, doi:10.1007/s00340-009-3365-7, URL <https://doi.org/10.1007/s00340-009-3365-7>, 2009.

Zinner, T., Schwarz, U., Kölling, T., Ewald, F., Jäkel, E., Mayer, B., and Wendisch, M.: Cloud geometry from oxygen-A-band observations through an aircraft side window, *Atmospheric Measurement Techniques*, 12, 1167–1181, doi:10.5194/amt-12-1167-2019, URL <https://amt.copernicus.org/articles/12/1167/2019/>, 2019.

Statement of Authorship

I hereby declare that I have written this thesis independently and made no use of sources and aids other than those specified.

Paul Rothenberg
Leipzig, 2025-06-26